

Acoustic Streaming in High-speed Turbulent Channel Flow

Iman Rahbari*[†] and Guillermo Paniagua*

*Purdue University

School of Mechanical Engineering, Purdue University, West Lafayette, IN 47906

irahbari@purdue.edu · gpaniagua@purdue.edu

[†]Corresponding author

Abstract

In the present study, we use Direct Numerical Simulation to investigate the effect of acoustic streaming on the heat and momentum transfer within a compressible turbulent flow. A fully-developed channel flow at Reynolds number $Re_b = \bar{\rho}U_b\delta/\mu_w = 3000$ and $M_b = U_b/c_w = 0.75$ has been chosen as the test case wherein the acoustic pulsation is applied through an array of loudspeakers mounted on the side-walls. The optimal frequency and shape of excitation are found following an input/output analysis based on the Linearized Navier-Stokes Equations. The entire system resonates under such conditions which subsequently amplifies the acoustic waves up to over eight times. The acoustic streaming appeared as a result of non-linear interaction between turbulent flow and acoustic waves enhances the heat transfer rate at a rate higher than the skin friction. This technique opens new avenues towards enhancing the efficiency of heat exchangers with minimal increase in pressure losses.

1. Introduction

Acoustic streaming refers to a physical process where an oscillating wave drives a steady fluid motion. By passage of an acoustic wave over a wall, a thin oscillatory layer with thickness $\delta_s = \sqrt{2\nu/\omega}$ forms near the boundary, called the Stokes layer, wherein the viscous effects on the waves decay exponentially. In this relation, ν denotes the dynamic viscosity and ω represents the frequency of oscillations. Stokes layer interacts with the background boundary layer which, under specific conditions, may lead to acoustic streaming.

One major contributing parameter in this process is the frequency of oscillations. If the background flow is turbulent, depending on such frequency, different responses may be observed. At high frequencies, edge of the Stokes layer, δ_s , falls within the viscous sub-layer. This case is referred to as "quasi-laminar" where the acoustic wave interacts with the flow only through time-averaged flow quantities. On the other hand, at low oscillation frequencies, Stokes layer thickness goes beyond the laminar sub-layer, where turbulent mixing becomes relevant. In this case, turbulent time-scales may be significantly shorter than the wave's period which marks the "quasi-steady" regime.¹⁸ The second parameter corresponds to the relative amplitude of the oscillations, i.e. $a_w = U_w/U_b$, where U_b and U_w respectively represent the bulk background velocity and velocity oscillation amplitude. Lodahl et al³ concluded that the changes in time-averaged skin friction, essentially due to the streaming effects, may appear where this parameter is larger than 1. Scotti and Piomelli¹³ had similar observations, as well.

Recently, Agarwal et. al studied the acoustic streaming and its effect on forced convection via a multi-fidelity approach.¹ They reported that, under specific conditions, such phenomenon may enhance the heat transfer at a rate higher than the skin friction violating the Reynolds stress analogy. In the present paper, we build upon these results and extend the analysis within the high-speed turbulent channel flow configuration. We identify the optimal conditions to create acoustic resonance within the domain in order to promote the non-linear interaction between the background flow and perturbations. We also study the effect of acoustic forcing amplitude on the temporal evolution of perturbation as well as streaming quantities. This research is a step towards demonstrating the *acoustic streaming* as a new way to effectively enhance the heat transfer rate in the heat exchangers without substantial skin friction losses.

2. Numerical tools

Navier-Stokes equations for a fully-compressible flow can be written in the dimensionless form as,

STREAMING IN HIGH-SPEED CHANNEL FLOW

$$\begin{aligned}
\frac{\partial \rho}{\partial t} + \frac{\partial}{\partial x_j}(\rho u_j) &= 0 \\
\frac{\partial}{\partial t}(\rho u_i) + \frac{\partial}{\partial x_j}(\rho u_i u_j) &= -\frac{\partial p}{\partial x_i} + \frac{1}{Re} \frac{\partial}{\partial x_j}(\tau_{ij}) + f_i \delta_{1i} \\
\frac{\partial E}{\partial t} + \frac{\partial}{\partial x_j}[(E + p)u_j] &= \frac{1}{RePr} \frac{\partial}{\partial x_j} \left(k \frac{\partial T}{\partial x_j} \right) + \frac{1}{Re} \frac{\partial}{\partial x_k} (\tau_{jk} u_j) + f_i u_i \delta_{1i}
\end{aligned} \tag{1}$$

where x_1 , x_2 , and x_3 denote the streamwise (x), wall-normal (y), and spanwise (z) directions. All spatial coordinates are made dimensionless with respect to the channel half width δ . Temperature, density and velocity are respectively scaled with wall temperature T_w , bulk density ρ_b and speed of sound at wall temperature c_w as reference values. Last term on the right hand side of momentum and energy equations are the source terms employed to keep the mass flow-rate constant in the present flow configuration as well as to mimic the effect of loudspeakers on the flow. Total energy (E) and viscous stress tensor (τ^{ij}) are expressed as:

$$E = \frac{p}{\gamma - 1} + \frac{1}{2} \rho u_i u_i, \quad \tau_{ij} = \mu \left(\frac{\partial u_i}{\partial x_j} + \frac{\partial u_j}{\partial x_i} - \frac{2}{3} \frac{\partial u_k}{\partial x_k} \delta_{ij} \right) \tag{2}$$

where the exponential form $\mu/\mu_w = (T/T_w)^{0.7}$ is employed to determine the molecular viscosity at any given temperature. Prandtl number is set to $Pr = 0.72$ and ideal-gas equation of state $p = \rho RT$ is adopted for Air. We use a sixth-order staggered finite difference method⁵ for spatial discretization of these equations along with a third-order Runge-Kutta method for time-advancement.

2.1 Validation

We study supersonic turbulent flow in a channel configuration to assess the accuracy of our numerical tool. We assume the boundary layer to be fully developed in the streamwise direction. Periodic boundary condition is also applied along the spanwise direction. Reynolds number is fixed at $Re_b = \bar{\rho} U_b \delta / \mu_w = 3000$ and Mach number is set to $M_b = U_b / c_w = 1.5$. The computational domain of size $L_x \times L_y \times L_z = 4\pi\delta \times 2\delta \times 1.5\pi\delta$ is discretized using $N_x \times N_y \times N_z = 144 \times 128 \times 96$ grid points which translates into the grid resolution of $(\Delta x^+, \Delta y^+_{min}, \Delta z^+) \approx (17, 0.21, 9.7)$ based on wall units, e.g. $y^+ = \rho_w u_{\tau} y / \mu_w$. Time-averaged streamwise velocity, density, and temperature profiles as well as RMS value of fluctuating velocity components are plotted in figure 1. Reference data taken from the DNS study of Coleman et al² is also included in this figure showing an excellent agreement with results of our numerical tool.

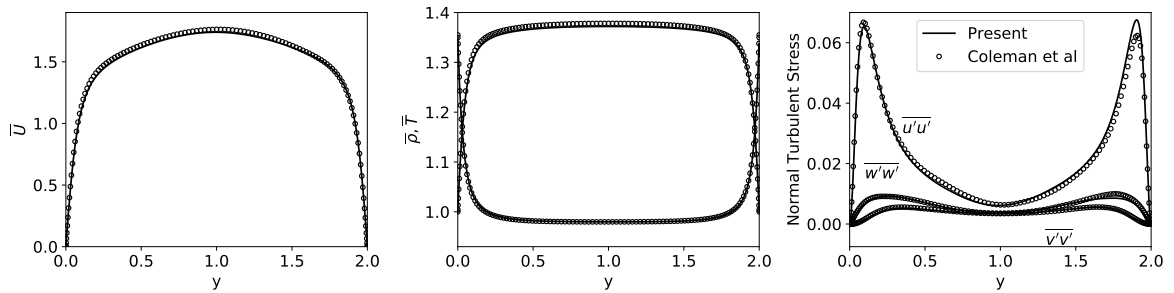


Figure 1: Time-averaged streamwise velocity (left), density and temperature (middle), and normal Reynolds Stress components (right) for a fully developed turbulent flow in a channel at $Re_b = 3000$ and $M_b = 1.5$. Circles are taken from DNS of Coleman et al² and line shows results of the represent the present

3. Flow configuration

In the present paper, we study the interaction of an external acoustic wave and a fully-developed turbulent compressible boundary layer within a channel geometry. To aim this, we propose a computational setup schematically presented in figure 2. It resembles the flow in a duct where loudspeakers are placed on a narrow region on the side walls. To avoid complexities associated with the corners, we only model the region near the mid-span. Therefore, we may assume

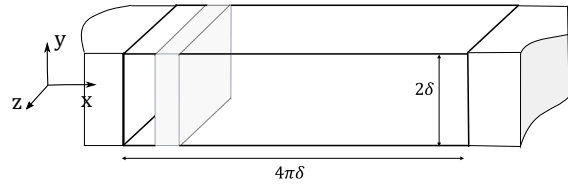


Figure 2: Schematic view of computational setup. Forcing of form Eq. 3 is active only in the shaded area.

periodicity in spanwise direction. To model the effect of loudspeaker on the flow in this region, we implement a forcing function of form 3. This is essentially a streamwise time-periodic force that follows a Gaussian distribution in x -direction and is only active within the shaded region. We assume to have repeatedly stacked a few of such units together, hence only one segment is simulated and the periodic boundary condition is applied in the streamwise direction.

$$\vec{f}_f(\mathbf{x}, t) = A_f \exp\left(-\frac{(x - x_m)^2}{L_f^2}\right) \sin(\omega_f t) \vec{e}_x \quad (3)$$

where L_f corresponds to the length of the region where forcing is applied and x_m denotes the x -coordinate of this region's mid-point. These two parameters are assumed constant in this study $L_f = 0.05L_x$ and $x_m = 1.75\delta$.

4. Linear analysis

Recent numerical techniques proposed to characterize unsteady flows are diverse in their origins and primary applications; the majority rely on time-resolved observations, e.g. Spectral Proper Orthogonal Decomposition¹⁴ and Dynamic Mode Decomposition¹¹ which limits their *predictive* applications, while others, on the other hand, target fundamental problems via classic approaches like Triple-Deck Theory.^{10,16} Linear Stability Analysis was originally introduced to characterize the onset of transition to turbulence (in both incompressible¹² and compressible⁴ regimes), but lately has been employed to predict and control low-frequency flow features in laminar flows.¹⁵ Recent efforts have suggested taking time-averaged (mean) flow quantities as *the equilibrium state* and extend such analysis to include the turbulent flow applications.^{6,7,9} The present research follows the same approach to analyze the unexcited turbulent flow and select the optimal frequency of excitation.

4.1 Linear Stability Analysis

Linearized Navier-Stokes equations are derived by decomposing a flow variable $q(x, t)$ to an equilibrium state, $\bar{q}(x)$, (or base flow) and small perturbations, i.e. $q(\mathbf{x}, t) = \bar{q}(\mathbf{x}) + \varepsilon q'(\mathbf{x}, t) + O(\varepsilon^2)$. Applying this expansion to Navier-Stokes equations (1) and retaining only the first order perturbations gives:

$$\mathcal{B} \frac{dq'}{dt} = \mathcal{A} q' \quad (4)$$

where \mathcal{A} and \mathcal{B} are time-independent operators that contain the base flow quantities as well as spatial derivatives.¹⁷ We assume the solution to this ODE takes the form $q'(\mathbf{x}, t) = \hat{q}(\mathbf{x}) \exp(-j\omega t)$ which simplifies the equation (4) into a generalized eigenvalue problem:

$$-j\omega \mathcal{B} \hat{q} = \mathcal{A} \hat{q} \quad (5)$$

where ω is the complex angular velocity. In the present work, base flow as well as boundary conditions are homogeneous in streamwise and spanwise directions, therefore the perturbation form is simplified to $q'(\mathbf{x}, t) = \hat{q}(y) \exp(jk_x x + jk_z z) \exp(-j\omega t)$ where k_x and k_z are streamwise and spanwise wavenumbers, respectively. The equilibrium state, $\bar{q}(\mathbf{x})$, is found via time-averaging of the unexcited flow quantities. We also target 2D modes (xy -plane) in the present analysis, and therefore, $k_z = 0$ is adopted. We use the Chebyshev spectral method to discretize the spatial derivative terms in operators \mathcal{A} and \mathcal{B} .⁸

4.2 Input-output analysis

Applying a harmonic forcing of $f'(\mathbf{x}, t) = \hat{f}(\mathbf{x}) \exp(-j\omega t)$ to the linearized Navier-Stokes equation (4) makes up a non-homogeneous ODE following:

$$\mathcal{B} \frac{dq'}{dt} = \mathcal{A}q' + f' \quad (6)$$

We can write the solution in terms of the input forcing and simplify as:

$$\hat{q} = \mathcal{H}(\omega) \hat{f} \quad \text{where} \quad \mathcal{H}(\omega) = (-j\omega \mathcal{B} - \mathcal{A})^{-1} \quad (7)$$

and therefore, $\mathcal{H}(\omega)$ acts as a transfer function mapping the input to the solution. The growth rate in this dynamical system is:

$$R(\omega) = \frac{\|q'\|}{\|f'\|} = \frac{\|\mathcal{H}(\omega)\hat{f}\|}{\|\hat{f}\|} \leq \|\mathcal{H}(\omega)\| \quad (8)$$

Singular Value Decomposition (SVD) of this operator yields:

$$\mathcal{H}(\omega) = U \Sigma V^* \quad (9)$$

where U and V are left and right singular vectors of $\mathcal{H}(\omega)$ and Σ is a diagonal matrix with the corresponding singular values in descending order. It can be shown that $\|\mathcal{H}(\omega)\| \leq \sigma_1$ where σ_1 is the largest singular value of this matrix. Therefore, following the equation (9), we can write $\mathcal{H}(\omega)v_1 = u_1\sigma_1$ indicating that, at angular velocity ω , the maximum growth rate is σ_1 , optimal forcing distribution is the first right singular vector v_1 and the optimal response would be the first left singular value u_1 .

In the present flow study, we assume $Re_b = 3000$ and $M_b = 0.75$. All other computational parameters are remained similar to the section 2.1. Upon calculating the time-averaged, velocity, temperature and density profiles, the optimal growth rate (equation 7) for a range of real-valued angular velocity are plotted in figure 3. In these calculation,s we only consider the smallest wavelength that is accommodated within our domain of size 4π , i.e. $k_x = 0.5$. The optimal

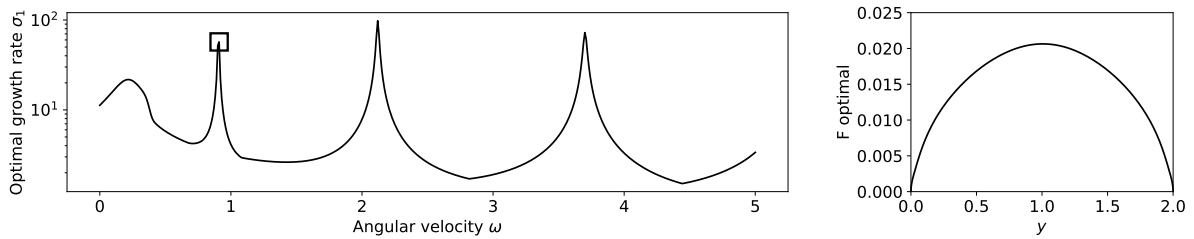


Figure 3: The optimal growth rate at different real-valued angular velocities (left) along with the optimal forcing associated with the first peak (right) denoted the block symbol. Calculations are performed at $Re_b = 3000$ and $M_b = 0.75$ and assuming $k_x = 0.5$

condition associated with the first large peak of σ_1 , denoted by the block symbol, has been selected to create resonance in the flow. The optimal forcing distribution at this frequency is shown in figure 3 (right). However, for simplicity and ease of replicability in experiments, we only assume a uniform forcing distribution in wall-normal direction.

5. Fully non-linear analysis

Fully compressible Navier-Stokes equations 1 along with the forcing function 3 are numerically solved in this section. In all calculations, $M_b = U_b/c_w = 0.75$ and $Re_b = \rho_b U_b \delta / \mu_w = 3000$ remain constant. Operating condition for these calculations are reported in table 1.

5.1 Transient growth of a resonating acoustic wave in compressible turbulent channel flow

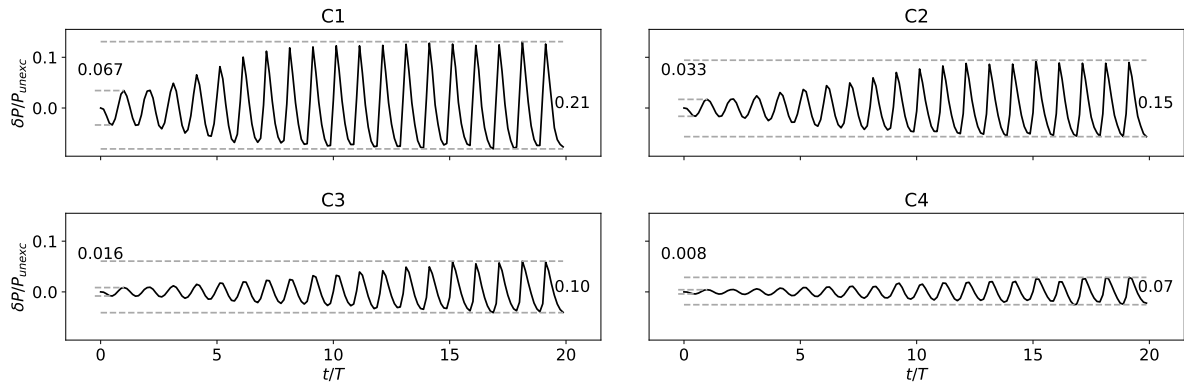
Applying the forcing function 3 generates time-periodic sinusoidal fluctuations super-imposed on the background turbulent flow field. In order to effectively analyze the dynamics of such perturbations, we take:

$$q_{exc} = q_{unexc} + \delta q \quad (10)$$

Case number	A_f	ω_f	$G = \delta p_{\text{limit-cycle}}/\delta p_{\text{initial}}$	$\delta_s^+ = \delta_s u_\tau/\nu_w$
C1	0.250	$2\pi/6.94$	3.12	4.23
C2	0.125	$2\pi/6.94$	4.53	4.23
C3	0.062	$2\pi/6.94$	6.39	4.23
C4	0.031	$2\pi/6.94$	8.77	4.23

Table 1: Simulation parameters for non-linear analysis of acoustic excitation

where q_{exc} is a generic flow quantity taken from the excited flow simulations (C1 to C4 cases in table 1) and q_{unexc} represents the same quantity extracted from the unexcited base flow calculations. These two simulations have identical grid and time-step sizes and are initialized with identical flow fields in order to minimize the artificial numerical effects. Figure 4 illustrates the pressure perturbations δp for the first 20 excitation periods at center of the forcing region ($y = 1$). This quantity is averaged in $x \in [1.05 - 2.55]$ and along the spanwise direction. Initially, the perturbations are relatively weak and, therefore, interact linearly with each other as well as the background flow. This can be observed as pure sinusoidal oscillation in the first few periods. In C1 to C4 cases, amplitude of oscillations grow exponentially manifesting the *resonance* under the corresponding operating conditions. Stronger perturbations cause *greater non-linear interactions* within the domain which essentially distributes the perturbation energy among multiple frequencies. This appears as more skewed oscillations in pressure perturbations. After few excitation periods, the amplitude growth slows down and eventually leads to sustained limit-cycle oscillations. Gain achieved through the resonance mechanism,

Figure 4: Pressure fluctuations $\delta p = p_{exc} - p_{unexc}$ at the center of the forcing region, $y = 1$, spatially averaged within $x \in (1.05, 2.55)$ and $z \in (0, 1.5\pi)$ normalized by the pressure value at the unexcited case at the same position

$G = \delta p_{\text{limit-cycle}}/\delta p_{\text{initial}}$, varies depending on the initial amplitude. This is evident by considering the initial and limit-cycle perturbation amplitudes of C1 to C4 cases reported in figure 4. At high A_f values, the initial perturbation amplitude is larger and non-linear effects dominate the oscillation dynamics faster and therefore, limit-cycle oscillation is reached in fewer periods. Results indicate that by doubling the A_f , initial pressure perturbation amplitude $\delta p_{\text{initial}}$ doubles while the corresponding limit-cycle amplitude $\delta p_{\text{limit-cycle}}$ approximately scales with $\propto \sqrt{A_f}$ resulting in the net gain following,

$$G = \frac{\delta p_{\text{limit-cycle}}}{\delta p_{\text{initial}}} \propto \frac{1}{\sqrt{A_f}}, \quad \text{if } A_f \neq 0 \quad (11)$$

We also investigate the overall effect of excitation on the near-wall heat and momentum transport by looking at the spatially-averaged skin friction (C_f) and Nusselt numbers (Nu) in time, where

$$C_f = \frac{\mu_w \frac{\partial U}{\partial y}|_w}{0.5\rho U_b^2} \quad \text{and} \quad \text{Nu} = \frac{\frac{\partial}{\partial y}(T - T_w)|_w}{(T_b - T_w)/\delta}. \quad (12)$$

We define two parameters, Shear and Thermal Enhancement Factor, respectively SEF and TEF, following:

$$\text{SEF} = \frac{C_{f,\text{excited}}}{C_{f,\text{unexcited}}}, \quad \text{TEF} = \frac{\text{Nu}_{\text{excited}}}{\text{Nu}_{\text{unexcited}}} \quad (13)$$

STREAMING IN HIGH-SPEED CHANNEL FLOW

which are essentially relative skin friction or Nusselt number of the excited flow divided by the corresponding value in the unexcited condition. Figure 5 illustrates the instantaneous SEF (dashed lines) and TEF (solid lines) at C1 to C4 for the first 60 cycles.

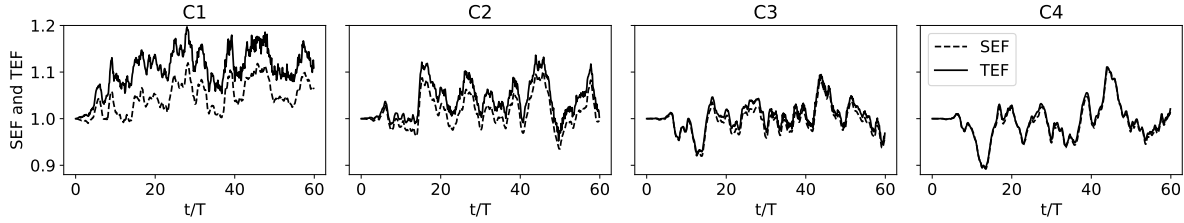


Figure 5: Instantaneous Thermal (solid line) and Shear enhancement factors (dashed-lines) for C1 to C4 spatially averaged at each time-step over the entire bottom wall.

As per definition, these two parameters start from the unity. In case C4 with the smallest excitation amplitude, SEF and TEF show almost identical behavior in time which indicates that momentum and heat transport processes, under the corresponding condition, are closely coupled. By increasing the excitation amplitude (from right to left), these two parameters substantially deviate, although following a similar trend. It suggests that such excitation effectively energizes the heat transfer process while affecting the momentum transport to a lesser degree. This introduces a novel technique to enhance the heat transfer rate in heat exchangers with minimal penalty in skin friction losses.

5.2 Time-averaged flow quantities

This section focuses on the time-averaged flow quantities in order to study the streaming phenomenon. Figure 6 shows a close-up view of the streaming temperature, $T_{st} = \bar{T}_{excited} - \bar{T}_{un-excited}$ near the bottom wall for cases C1 to C4. All cases exhibit regions with positive and negative T_{st} , relative to the background temperature field. At low excitation amplitudes, e.g. case C4, this pattern is spatially periodic with only one dominant streamwise wavenumber $k_x = 8$, while at higher amplitudes like C1, more harmonics with $k_x = 16, 24, 32$ also appear. This is in agreement with the observations in figure 4 where at higher A_f 's, a sharper change of perturbation is seen across one perturbation passage that indicates the presence of higher harmonics of the excitation frequency in the perturbations signal. The substantial

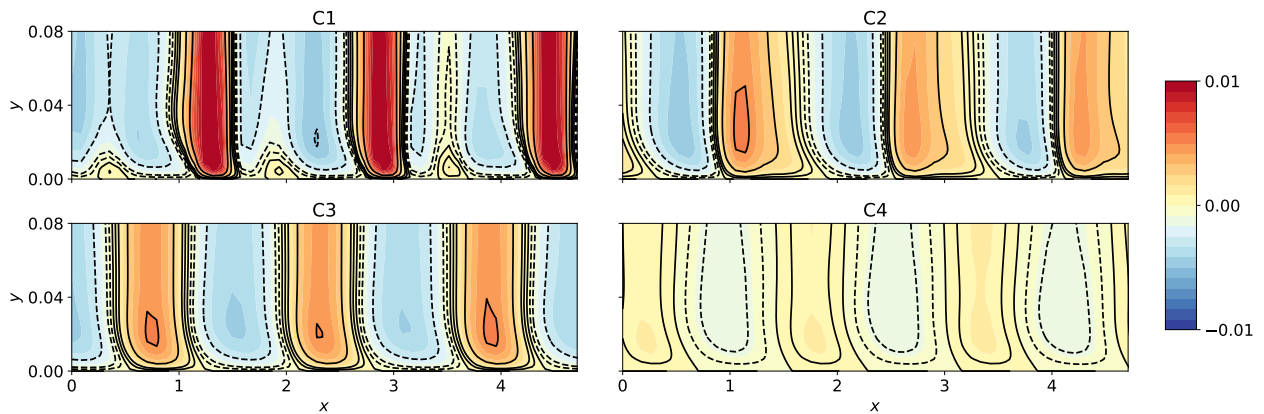


Figure 6: Streaming temperature contour at four different cases introduced in table 1. Temperature is normalized with wall temperature. Contours are capped at ± 0.01 for better representation

temperature jump in C1, noted in initial phases of each period, is translated into narrow, yet intense regions of positive T_{st} in figure 6. Upon time integration of Shear and Thermal Enhancement factors for cases C1 to C4, net changes in skin friction coefficient and Nusselt number due to acoustic streaming are tabulated in 2. We also introduce an effectiveness factor as $\eta = (TEF - 1)/(SEF - 1)$ which emphasizes the gain in heat transfer rate compared to the losses in skin friction. In C1 and C2 cases, we observe a heat transfer enhancement that is 2-3 times larger than the corresponding cost in friction drag suggesting the significant potential of using streaming under such conditions in heat exchangers. Acoustic excitation in C3 and C4 cases resulted in minimal ($< \pm 1\%$) streaming effects on Nu and C_f which is prone to numerical artifacts, therefore the effectiveness factor is not reported for these cases.

	C1	C2	C3	C4
Change in Nu	+10.53%	+4.01%	+0.39%	-0.39%
Change in C_f	+4.67%	+1.43%	-0.56%	-0.78%
Effectiveness factor (η)	2.26	2.81	N/A	N/A

Table 2: The net effect of acoustic streaming on Nu and C_f over the entire bottom wall, temporally averaged over 60 cycles

To inspect the impact of excitation on turbulence, we consider the second-order time statistics and investigate the turbulent velocity fluctuations in streamwise and spanwise direction as well as temperature fluctuations in figure 7. Although figure 6 suggests a streamwise periodic pattern for streaming flow, we focus on the spatially averaged-statistics as it effectively represents the net effect on turbulence within the whole domain. Results indicate that increasing the exci-

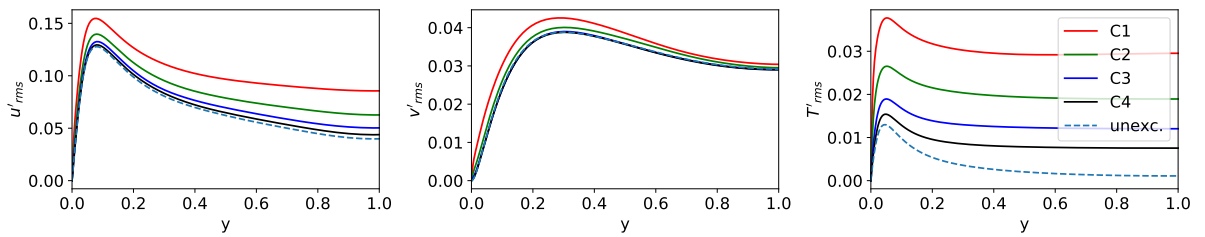


Figure 7: A comparison between the RMS value of turbulent fluctuations in the excited flow at different amplitudes. Dashed-line indicates the reference results taken from the base flow calculations

tation amplitude has the largest impact on temperature fluctuations. It intensifies the near-wall peak (almost linearly following $\Delta T' = T'_{excited,rms} - T'_{unexcited,rms} \propto A_f$) while also raising the temperature fluctuations at the core of the channel at a faster rate (which scales non-linearly with A_f). Similar streaming effect, however less pronounced, can be observed on u'_{rms} . On the other hand, wall-normal fluctuations are the least altered by streaming, such that only results from C1 and C2 (with the highest excitation amplitudes) visibly deviate from the corresponding values in the unexcited case. This can be attributed to the uniformity of forcing distribution (equation 3) in this direction. As such, considering the figure 7, a larger streaming effect is expected on the wall-normal heat flux compared to the shear stress which agrees with data reported in table 2.

6. Conclusion

In this research, we used high-fidelity numerical simulations to study the interaction between acoustic wave and high-speed turbulent boundary layer. To aim this, we proposed a computational setup which resembles the flow in a duct with acoustic drivers on the side walls. To promote the non-linear interaction between the acoustic wave and background flow, we used Linear Stability Analysis and determined the optimal parameters for creating acoustic resonance in the flow. Under such conditions, we extensively analyzed the effect of perturbation amplitudes on the resulting acoustic streaming through parameters including Shear and Thermal Enhancement Factors (SEF and TEF) as well as turbulent fluctuating velocity and temperature. Results suggested that acoustic streaming, under favorable conditions, can enhance the heat transfer rate with minimal increase in skin friction which can be used to optimize the existing heat exchangers.

7. Acknowledgments

Authors would like to thank Prof. Sanjiva Lele for granting access to an early version of CFDSU code. This research was supported by Grant No 2016358 from the Binational Science Foundation. Numerical simulations were performed in part using the Extreme Science and Engineering Discovery Environment (XSEDE) Comet at SDSC and Bridges at PSC through allocation TG-CTS170041 and, partially on AWS cloud infrastructure supported by AWS Cloud Credits for Research program.

References

- [1] Tapish Agarwal, Iman Rahbari, Jorge Saavedra, Guillermo Paniagua, and Beni Cukurel. Multi-fidelity analysis of acoustic streaming in forced convection heat transfer. In *ASME Turbo Expo 2019: Turbomachinery Technical Conference and Exposition*. American Society of Mechanical Engineers, 2019.
- [2] Gary N Coleman, John Kim, and RD Moser. A numerical study of turbulent supersonic isothermal-wall channel flow. *Journal of Fluid Mechanics*, 305:159–183, 1995.
- [3] CR Lodahl, B Mutlu Sumer, and Jørgen Fredsøe. Turbulent combined oscillatory flow and current in a pipe. *Journal of Fluid Mechanics*, 373:313–348, 1998.
- [4] Mujeeb R Malik. Numerical methods for hypersonic boundary layer stability. *Journal of computational physics*, 86(2):376–413, 1990.
- [5] Santhanam Nagarajan, Sanjiva K Lele, and Joel H Ferziger. A robust high-order compact method for large eddy simulation. *Journal of Computational Physics*, 191(2):392–419, 2003.
- [6] Mahesh Natarajan, Jonathan B Freund, and Daniel J Bodony. Actuator selection and placement for localized feedback flow control. *Journal of Fluid Mechanics*, 809:775–792, 2016.
- [7] Joseph W Nichols, Johan Larsson, Matteo Bernardini, and Sergio Pirozzoli. Stability and modal analysis of shock/boundary layer interactions. *Theoretical and Computational Fluid Dynamics*, 31(1):33–50, 2017.
- [8] Iman Rahbari and Carlo Scalo. Linear stability analysis of compressible channel flow over porous walls. In *Whither Turbulence and Big Data in the 21st Century?*, pages 451–467. Springer, 2017.
- [9] Iman Rahbari and Carlo Scalo. Quasi-spectral sparse bi-global stability analysis of compressible channel flow over complex impedance. In *55th AIAA Aerospace Sciences Meeting*, page 1879, 2017.
- [10] Amir S Rezaei and Haitham E Taha. Transition regime and its effects on the unsteady aerodynamic characteristics of a pitching airfoil. In *AIAA Scitech 2019 Forum*, page 0302, 2019.
- [11] Peter J Schmid. Dynamic mode decomposition of numerical and experimental data. *Journal of fluid mechanics*, 656:5–28, 2010.
- [12] Galen Brandt Schubauer and Harold Kenneth Skramstad. Laminar-boundary-layer oscillations and transition on a flat plate. Technical report, NATIONAL AERONAUTICS AND SPACE ADMINISTRATION WASHINGTON DC, 1948.
- [13] Alberto Scotti and Ugo Piomelli. Numerical simulation of pulsating turbulent channel flow. *Physics of Fluids*, 13(5):1367–1384, 2001.
- [14] Moritz Sieber, C Oliver Paschereit, and Kilian Oberleithner. Spectral proper orthogonal decomposition. *Journal of Fluid Mechanics*, 792:798–828, 2016.
- [15] Denis Sipp, Olivier Marquet, Philippe Meliga, and Alexandre Barbagallo. Dynamics and control of global instabilities in open-flows: a linearized approach. *Applied Mechanics Reviews*, 63(3):030801, 2010.
- [16] Haithem Taha and Amir S Rezaei. Viscous extension of potential-flow unsteady aerodynamics: the lift frequency response problem. *Journal of Fluid Mechanics*, 868:141–175, 2019.
- [17] V Theofilis and T Colonius. Three-dimensional instabilities of compressible flow over open cavities: direct solution of the biglobal eigenvalue problem. *AIAA Paper*, 2544:2004, 2004.
- [18] Chenyang Weng, Susann Boij, and Ardeshir Hanifi. Numerical and theoretical investigation of pulsatile turbulent channel flows. *Journal of Fluid Mechanics*, 792:98–133, 2016.